Research Article | Vol. 9, No. 8 / 1 August 2019 / Optical Materials Express 3504
Optical Materials EXPRESS

Pump-power-dependence of a $CsPbBr_3$-in-Cs_4PbBr_6 quantum dot color converter

MIGUEL F. LEITÃO,[1] M. S. ISLIM,[2] L. YIN,[2] S. VIOLA,[3] S. WATSON,[3] A. KELLY,[3] Y. DONG,[4] X. LI,[4] H. ZENG,[4,5] S. VIDEV,[2] H. HAAS,[2] E. GU,[1,6] I. M. WATSON,[1] N. LAURAND,[1,7] AND M. D. DAWSON[1]

[1]*Institute of Photonics, Department of Physics, SUPA, University of Strathclyde, Glasgow, United Kingdom*
[2]*Li-Fi R&D Centre, Institute for Digital Communications, University of Edinburgh, Edinburgh, EH9 3JG, United Kingdom*
[3]*Electronic & Electrical Engineering, University of Glasgow, Glasgow, United Kingdom*
[4]*Institute of Optoelectronics and Nanomaterials, College of Material Science and Engineering, Nanjing University of Science and Technology, Nanjing 210094, China*
[5]*zeng.haibo@njust.edu.cn*
[6]*erdan.gu@strath.ac.uk*
[7]*nicolas.laurand@strath.ac.uk*

Abstract: A detailed study of the pump-intensity dependent characteristics of an all-inorganic $CsPbBr_3$-in-Cs_4PbBr_6 quantum dot (QD) color converter are reported. This is an attractive material to color convert UV/blue GaN optical pump sources for digital lighting applications, e.g. visible light communications (VLC). It demonstrates narrow spectral emission (522 nm peak emission and < 20 nm full-width-at-half-maximum), invariant with the pump power density (from 0 to 7.15 kW/cm^2). The optical bandwidth increases, from 10 MHz at 300 μW/cm^2, up to 22 MHz at 3 W/cm^2, and 41 MHz at 7.15 kW/cm^2. This acceleration of the emission is ascribed to both an increase of the radiative decay rate in the low-pump-density regime, and to the emergence of non-radiative pathways at higher pump density. The higher bandwidth at high-pump density enables a 30% increase in the data rate of a free space VLC link using this color converter.

1. Introduction

Luminophores pumped by efficient blue GaN lasers or LEDs are enabling solid-state optical sources for displays, lighting and illumination, and they now have a role to play in emerging digital lighting applications, such as visible light communications (VLC) [1,2]. In this context, alternatives to phosphors, typically used for color conversion of GaN devices, are being explored to address the bandwidth issue of phosphor-converted sources that severely limits their capability [3,4]. These alternatives include semiconductor quantum well structures [5,6], organic semiconductors [7] and quantum dots (QDs) [8–10]. The latter are particularly attractive, combining high efficiency, narrow emission linewidth and faster dynamics than conventional phosphors, partly thanks to enhanced density of states and electron/hole wavefunction overlap [11]. The luminescence lifetime of QDs is wavelength- and alloy-dependent and perovskite semiconductor QDs, first reported only 4 years ago [12], promise the shortest lifetimes and consequently the fastest color conversion dynamics [11].

All-inorganic metal halide perovskite colloidal QDs of the form $CsPbX_3$ (X = Cl, Br or I or a combination thereof) were first reported by Protesescu et al. [12], enabling efficient

#369752 https://doi.org/10.1364/OME.9.003504
Journal © 2019 Received 12 Jun 2019; revised 19 Jul 2019; accepted 21 Jul 2019; published 29 Jul 2019

Optical Materials EXPRESS

emission across the visible spectrum, and have since been demonstrated in LEDs [13] and even as color converters for VLC [9,10]. When prepared as colloidal dispersions, these QDs are invariably stabilized by an organic ligand shell surrounding the inorganic core, and the term 'all-inorganic' refers to the absence of organic cations in the core [14–17]. A disadvantage of these conventional perovskite QDs is their limited thermal and moisture stability although approaches can mitigate the issue [14,18]. On the other hand, reports on Cs_4PbBr_6 have shown that this material can exhibit highly efficient green luminescence and enhanced stability [19]. Cs_4PbBr_6 does not have a perovskite structure but is sometimes called 0D perovskite by analogy because $[PbX_6]^{4-}$ octahedrons are isolated in the crystal, resulting in a higher bandgap than for $CsPbX_3$, and giving band edge emission in the UV. The origin of the green luminescence has therefore been the subject of extensive debate in the literature. The most plausible explanation is the formation of $CsPbBr_3$ QDs within the Cs_4PbBr_6 host, and we refer to this nanocomposite system as '$CsPbBr_3$-in-Cs_4PbBr_6' QDs in the following discussion. Strong arguments for this nanostructure and origin of the green luminescence were presented in Akkerman et al.'s paper, including a comprehensive critique of previous literature [20]. $CsPbBr_3$ QDs can form with an endoepitaxial relation to the host phase, and the $CsPbBr_3/Cs_4PbBr_6$ interface may have a large influence on their optical properties. Akkerman et al. note that most samples show luminescence spectra similar to colloidal $CsPbBr_3$ QDs 8-15 nm in diameter. They interpret the shift of emission from the blue to the green during growth of large Cs_4PbBr_6 crystals [21] as demonstrating thermodynamic instability of smaller $CsPbBr_3$ QDs formed initially. Other groups have also reported on the synthesis of similar materials with X-ray powder diffraction (XRPD) and transmission electron microscopy data supporting this $CsPbBr_3$ QDs in Cs_4PbBr_6 structure [21,22]. As a truly all-inorganic system, $CsPbBr_3$-in-Cs_4PbBr_6 QDs promise enhanced stability compared to colloidal quantum dots because the $CsPbBr_3$ QDs are 'ligand-free' and inherently encapsulated in a higher-bandgap semiconductor material. Indeed, this material was shown to have high thermal stability when demonstrated as a laser gain material [19]. In addition, the high dielectric constant of this environment is in principle beneficial to lower the QDs' radiative lifetime. These properties also make it very promising for green color-conversion in VLC-like applications. However, to our knowledge, it has never been studied in that context prior to this work.

Herein, we report on such $CsPbBr_3$-in-Cs4$PbBr_6$ QDs for fast color conversion, i.e. for applications necessitating higher bandwidth than could be obtained from typical phosphors. After a description of the materials and methods, we present in detail the dynamic optical characteristics for a 450 nm pump power density up to 7.15 kW/cm^2. This range covers the likely pump density regimes when implemented with GaN LEDs and laser diodes in applications. Prior work on color conversion for VLC often overlooked the effect of the excitation density, which can be critical for QDs as we will demonstrate in this paper. Building on our study of photophysical properties, a free space point-to-point VLC link was demonstrated with the $CsPbBr_3$-in-Cs4$PbBr_6$ QDs excited at two different density regimes, when pumped respectively with a 450 nm µLED and a 450 nm laser diode.

2. Material and methods

2.1. QD material and color converters

$CsPbBr_3$-in-Cs_4PbBr_6 QDs were grown by a room-temperature, non-aqueous solution method. More details on the synthesis, including XRPD characterization, can be found in [19,23]. The material consists of crystals with typical sizes up to hundreds µm and photoluminescence quantum yield (PLQY) up to 55% [19,23]. Figure 1(a) shows an example of such a crystal placed on a SEM sample holder and illuminated by UV light. The crystals were ground to a finer powder for further processing, leading to particle sizes of a few microns (see scanning electron microscope (SEM) images in Fig. 1(b)).

Optical Materials EXPRESS

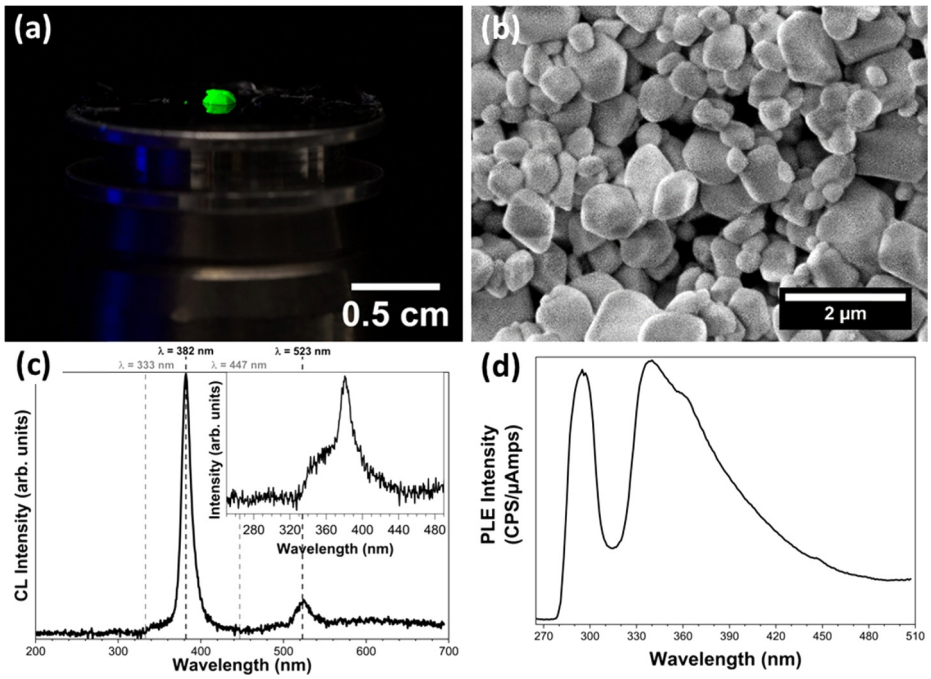

Fig. 1. (a) Image of a large crystal, under UV light excitation; (b) SEM image of crystal powder; (c) Normalized CL spectra from the surface of the crystal on top left; Inset: CL spectrum of the crystal on an area with less contribution from the 382 nm peak; (d) PLE of the powder in toluene (centered at 520 nm).

Cathodoluminescence (CL) measurements were conducted on the synthesized crystals using a homebuilt system based on a FEI Quanta 250 (environmental) SEM [24]. The crystal shown in Fig. 1(a) was imaged by SEM and the nominal 5×5 µm^2 area in the center of the picture was selected for CL analysis.

The resulting CL spectrum is presented in Fig. 1(c), where 3 different features are visible: a peak at 522 nm; a peak at 382 nm; and a wide band between ~330 and 450 nm, visible in the inset (corresponding to an area with less contribution of the 382 nm peak). It is assumed that the broad band in the UV (330 - 450 nm) comes from radiative recombination involving the two lowest excited state levels of Pb^{2+}, as typically observed in Cs_4PbBr_6 [25], Cs_4PbCl_6 [26], KPb_2Cl_5 [27] and $RbPb_2Cl_5$ crystals [28]. The peak at 382 nm corresponds to the band-edge emission of Cs_4PbBr_6 [29]. The 522 nm peak is attributed to the confined $CsPbBr_3$ QDs.

Photoluminescence Excitation (PLE) analysis of the powder dispersed in toluene was also conducted using a Horiba Jobin-Yvon Fluorolog-3 spectrofluorometer. The emission at 520 nm was recorded while the excitation wavelength was scanned. The resulting profile can be observed in Fig. 1(d), in line with what was reported for colloidal Cs_4PbBr_6 [30,31]: the excitation profile increases below 510 nm until 340 nm, below which the excitation profile takes a dip centered at 315 nm, corresponding to the $1S_0 \rightarrow 3P_1$ transition of Pb^{2+} centers [32,33].

To prepare the color converting samples, the powder was mixed with poly(methyl methacrylate) (PMMA) inside a glass vial at a mass ratio of 20% (crystal powder to PMMA). Chloroform was added to the mix using a micro-pipette to achieve a final ratio of the mix to solvent of 250 mg/mL. A magnetic stirrer was placed inside the vial to mix the crystal powder, PMMA and chloroform, and left stirring overnight. 10 µL droplets of the solution were then poured onto a glass slide and left to dry in air; an example of one such sample can be observed in Fig. 2. After

Optical Materials EXPRESS

all measurements were done, the sample was cut in half, and photographed in cross-section, next to a silicon wafer. Knowing the silicon wafer thickness, the thickness at the center was estimated at 170 ± 15 µm. The extinction is ~80% for light at 450 nm. The absolute quantum yield of the sample at 1 W/cm^2 excitation density is 50%.

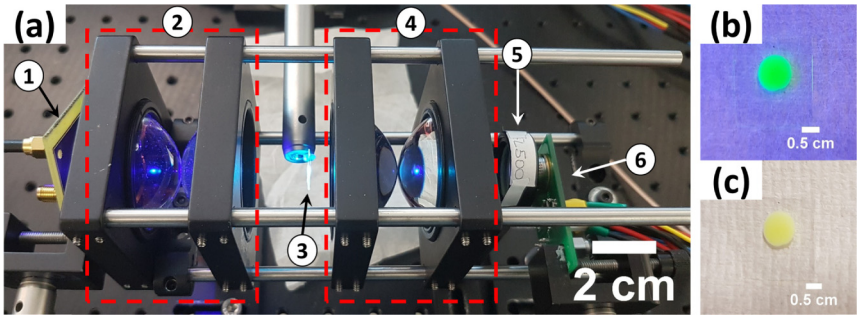

Fig. 2. a – Setup used for µLED pumped color conversion. The µLED's blue emission (1) is focused by two lenses (2) into a color converting sample (3). The sample's green emission is then focused by a second set of lenses (4), goes through an optical filter (5) that filters the blue emission and is detected by an APD (6), or other detector (power meter, spectrometer). Photographs of the sample under UV (b) and white light (c) illumination.

2.2. Color converter characterization set-ups

The color converter sample was characterized under both µLED and Laser Diode (LD) pumping (450 nm emission wavelength for both) for a pump power density ranging from just above 10 mW/cm^2 up to 7.15 kW/cm^2. Measurements taken include optical spectra, optical power and frequency response of the PL. These measurements and the associated set-ups are detailed next while results are shown and discussed in section 3.

The optical setup used for µLED pumping (Fig. 2(a)) consists of 2 aspheric lenses (diam. = 45 mm; f = 32 mm; NA = 0.612; AR coating 350-700 nm) used to image the emission of the µLED onto the color-converting sample (Figs 2(b) and 2(c) show the sample). A second set of lenses collects the sample emission in the forward direction onto the detector of choice for a specific type of measurement (optical power, spectrum or bandwidth). The set-up is slightly different for LD pumping in order to adjust the spot size, and hence the power density on the sample, while staying below the damage threshold of the PMMA composite (above 7.5 kW/cm^2). In that case, only one of the aspheric lenses described above focuses the LD emission on the sample, with the color-converted emission refocused by two aspheric lenses onto the detector.

The profile of the pump light (µLED and LD) hitting the sample was measured with a Thorlabs Camera Beam Profiler (BC106N-Vis-M). For the LD, the first order of the intensity profile in the vertical and horizontal transverse directions was fitted with a Gaussian function, and the distance between the two points of the function at $1/e^2$ of the maximum intensity was taken as double the waist of the beam for each direction ($2\omega_X$ and $2\omega_Y$ respectively). In the area defined by these points, 86% of the total power is accounted for, and the pump size A can be calculated according to [34] as:

$$A = \pi \cdot \omega_X \cdot \omega_Y \tag{1}$$

For the µLED, the profile data was best fitted with two cumulated Gaussian functions instead of one. We kept the definition of the beam width as the distance between the two points of intensity $1/e^2$ of the maximum of this combined fit; 77% of the total power is comprised within an enclosure of area A in this case. It should also be noted that we considered the average power

Optical Materials EXPRESS

density over the whole spot size, and not the power density on-axis (center of the beam), where the intensity is twice as high for a Gaussian beam.

From these measurements and calculations resulted two regimes of excitation in continuous wave illustrated in Fig. 3: one between 0.75-3.0 W/cm^2, for a µLED spot size of 0.3 mm^2 (Fig. 3(a)), and a second one between 1.05-7.15 kW/cm^2, for a LD spot size of 928 µm^2 (Fig. 3(b)). To account for beam divergence within the 170 µm thick sample and error in placing the sample at the focal point, the power density was averaged ± 500 µm either way of the focus along the optical axis. The power densities on the extremes of this range are 58% lower relatively to the focal power density, which is within the error bars for the power density at focal point.

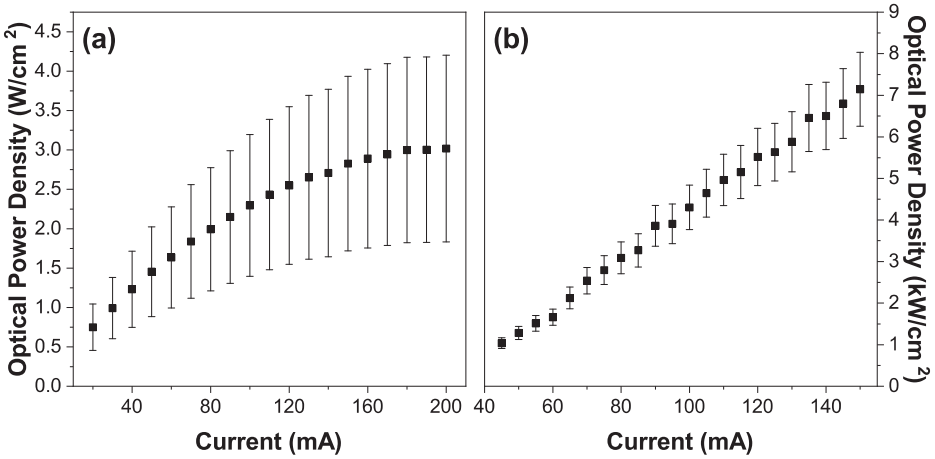

Fig. 3. Optical power density vs current for µLED (a) and LD (b).

The µLED was fabricated in house and has an emitting area of 100 x100 µm^2 [35], while the LD was an OSRAM PL450b. Both sources emit at 450 nm, in energy below the bandgap of bulk Cs_4PbBr_6 [16], hence $CsPbBr_3$ QDs are directly excited. A LabView script controlled a Yokogawa power source that drove the µLED, as well as a Thorlabs PM100A Coherent Power Meter connected to a C120VC power meter head (~94mm^2 active area) for optical power characterization of the sample under µLED pumping. The LD was driven by the same power supply and cooled with a Peltier cell and a TED200C temperature controller. A Newport 818 SL/DB silicon detector connected to a Newport 1830C power meter was used to collect the optical power from the LD and the color-converting sample excited by the LD. For the spectral characterization, a fiber-coupled spectrometer (Ocean Optics USB4000) was used in the place of the power meter.

The bandwidth measurements were performed using the same setups described above, but with a fast photoreceiver (Femto HAS-X-S-1G4-SI, bandwidth up to 1.4 GHz) detecting the emission of the color converter. The pump source (µLED or LD) was driven by an AC + DC signal. A power source supplied the DC signal to a Bias Tee, where it was added to the AC signal from an HP 8753ES S parameter Network Analyzer. This AC signal is a sine wave whose frequency is varied from 100 kHz to 1 GHz. The network analyzer reads the detector's response and compares it to the input signal, plotting the electrical power of the AC signal versus frequency. Varying the DC component between 20-200 mA (in 10 mA increments) for the µLED and 45-150 mA (in 5 mA increments) for the LD, the frequency response of the sample was characterized at different pump power densities.

The PL emission lifetime of the sample was also measured to estimate the bandwidth at a very low power density using a fluorescence lifetime spectrometer (Edinburgh Instruments mini-τ,

Optical Materials EXPRESS

Time Correlated Single Photon Counter – TCSPC). In this system the excitation source is a 128 ps pulsed diode laser (Edinburgh Instruments EPL 450 picosecond) with a 200 ns repetition rate. The excitation power density of the TCSPC LD at the sample was determined to be ~ 0.1 mW/cm^2 by the same method used previously for the μLED and LD.

2.3. Frequency response analysis

To retrieve the optical bandwidth of the color converter, the frequency response in dB of the pump source (μLED or LD) was removed from that of the color converter, and the result was fitted according to the model described below. The optical bandwidth is defined at the frequency at which the fitted electrical power data has dropped by 6 dB of the DC value. To analyze the frequency response (FR) of the sample, the model given in [36] was followed, where the FR of a color converter under modulated pump is given by (2),

$$FR(f) = 2 \cdot 10 \cdot Log\left(\sqrt{n(f)^2 + D(f)^2}\right) \tag{2}$$

where the terms $n(f)$ and $D(f)$ are given by (3) and (4):

$$n(f) = \frac{\sum_i \frac{\alpha_i \cdot \omega \cdot \tau_i^2}{1+\omega^2 \cdot \tau_i^2}}{\sum_i \alpha_i \cdot \tau_i} \tag{3}$$

$$D(f) = \frac{\sum_i \frac{\alpha_i \cdot \tau_i}{1+\omega^2 \cdot \tau_i^2}}{\sum_i \alpha_i \cdot \tau_i} \tag{4}$$

The multiplication by 10 and the logarithm in (2) serve to convert to decibels, while the x2 multiplication factor comes from the fact that $FR(f)$ is the electrical power of the AC amplitude. The optical bandwidth (f_{-6db}) versus excitation power density was extracted from this analysis. The average lifetime $\tilde{\tau}$ and optical bandwidth (f_{-6db}) are related by (5).

$$f_{-6db} = \frac{\sqrt{3}}{2 \cdot \pi \cdot \tilde{\tau}} \tag{5}$$

$\tilde{\tau}$ can be expressed as a set of n exponential decays, with respective lifetime τ_i and amplitude α_i , which also appear in (3) and (4), according to Eq. (6) [36]:

$$\tilde{\tau} = \sum_i^n \frac{a_i \cdot \tau_i^2}{a_i \cdot \tau_i} \tag{6}$$

Figure 4 shows examples of the FR of the color converter and respective fits for 1.3 and 7.15 kW/cm^2, for LD excitation. The FR and respective fittings are vertically shifted to provide a clear comparison between different excitation power densities. The model to fit the frequency response was applied assuming a triple exponential decay model, in line with the model used for TCSPC interpretation (see section 3). From the increase in power density it is evident that the bandwidth of the material increases as well, as the frequency response starts to drop at higher frequencies. The reasons for such behavior are detailed in section 3.2.

Optical Materials EXPRESS

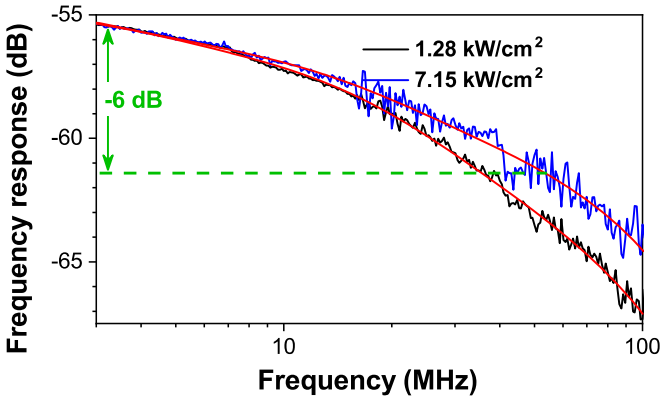

Fig. 4. Frequency response of the sample under LD excitation.

3. Results

3.1. Optical spectra and optical power

The emission spectrum of the sample was acquired at different excitation power densities. Under µLED excitation, the emission was centered at 522 nm, with a FWHM of 20 nm (not shown). Under LD excitation, the emission is centered at 521 nm for a FWHM of 18 nm (see Fig. 5). As the pump power density increases from 1.3 to 7.15 kW/cm^2, the spectrum remains stable, with the central peak shifting by less than 1 nm (inset of Fig. 5), which is below the resolution of the measurements. The FWHM broadens slightly to 20 nm. Such a narrow emission (~18 nm versus the 30 to 40 nm or more typical of II-VI or III-V QDs [37]) is ascribed to a small heterogeneous linewidth and is typical of $CsPbBr_3$ QDs. It is an advantage for color purity, but the key result here is that these spectral characteristics are stable over a wide range of pump densities. Such a stable emission spectrum is due to the electronic structure of $CsPbBr_3$ leading to a temperature independent band edge emission [19].

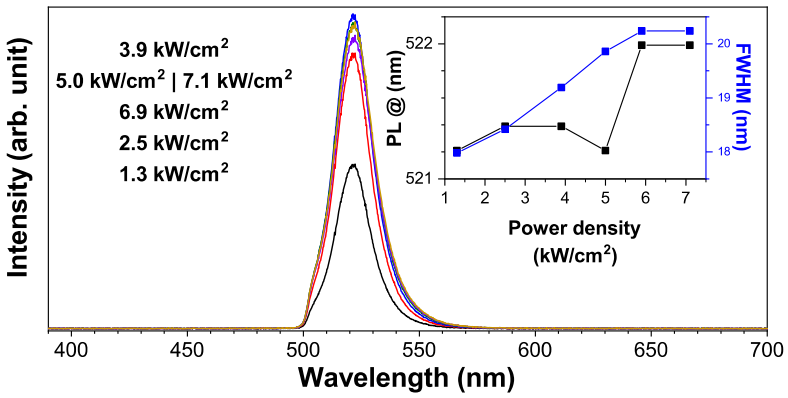

Fig. 5. Spectral emission under LD excitation for different power densities. Inset: position of the central maximum and FWHM for different power densities.

The relative efficiency of the sample is shown in Fig. 6(a) and its output power emitted in the forward direction and collected is plotted in Fig. 6(b) using a log-log scale. As the pump density increases, so does the color-converted power ('Optical power'). The slope of the linear fits at different power density regimes gives an indication of the dependence of the optical

Optical Materials EXPRESS

power on the pump density (linearly dependent on the carrier density), which follows a power law. At pump density below 3 W/cm^2, corresponding to μLED excitation, the slope is close to unity at 0.92 ± 0.04, indicating no change of the recombination dynamics within this range of power density. This is also consistent with the relative color conversion efficiency. The relative efficiency depends on the quantum efficiency (η), which is a function of the radiative recombination time (τ_r) and the non-radiative recombination time (τ_{nr}) [38]:

$$\eta = \frac{{\tau_r}^{-1}}{{\tau_r}^{-1} + {\tau_{nr}}^{-1}} \tag{7}$$

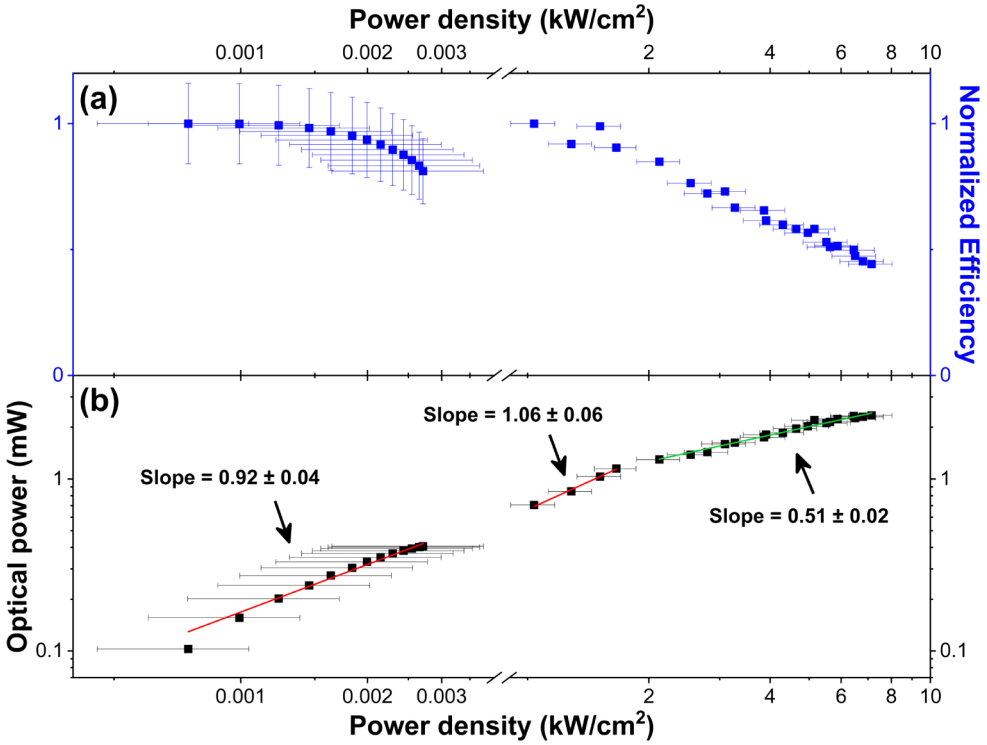

Fig. 6. (a) Normalized forward efficiency for μLED and LD. (b) Log-log plot of the optical power (black squares), vs pump power density for μLED (left) and LD (right); the linear fits (red and green) show the optical power follows a power law with excitation power density.

The denominator of Eq. (7) corresponds to the recombination rate, encompassing the radiative rate (${\tau_r}^{-1}$) and non-radiative recombination rate (${\tau_{nr}}^{-1}$). Even though not all light emitted from the sample is collected, the relative color conversion efficiency is defined as the ratio between output and absorbed optical power from the color converter; the latter being the output power from the pump multiplied by the sample's extinction at 450 nm. Because the relative efficiency is dependent on the set-up parameters it is here normalized to the highest efficiency value for both μLED and LD pumping regimes. It is plotted versus the excitation power density (Fig. 6(a)). Under μLED excitation, the relative efficiency is constant, within the ± 10% error margin. The apparent decrease of the values is attributed to small variation of the LED power calibration – however it is below the error margin. With the set-up, the relative forward efficiency is 10.1 ± 1.6%.

Under LD excitation, the optical power versus power density is linear up to 2 kW/cm^2, with a slope of 1.06 ± 0.06. It becomes sublinear for higher pump densities, the slope on the 2 kW/cm^2

Optical Materials EXPRESS

to 7.15 kW/cm^2 range being 0.51 ± 0.02. This behavior is indicative of a change in recombination dynamics, caused by a change in the ratio between radiative and non-radiative components, and the respective associated lifetimes. This change in recombination dynamics is also observable from the evolution of the relative color conversion efficiency: it drops by more than half from 1.0 (10.7 ± 0.1% forward efficiency) to 0.44 (4.7 ± 0.1% forward efficiency). We will see in section 3.2 that this behavior connects with an increase in the non-radiative recombination rate at high pump density.

In terms of power conversion performance under μLED pumping, these inorganic perovskite-based color converters perform similarly to green-emitting CdSSe/ZnS colloidal QDs tested under similar conditions [8]. At present, to our knowledge, there is no available data with which to compare the performance of these color converters under LD pumping.

3.2. Bandwidth characteristics

The color converter frequency response at different pumping density regimes is discussed here.

The bandwidth at the lowest pump density was obtained by TCSPC measurement. The PL decay of the sample was obtained by reconvoluting the instrument response and the sample's decay signal. A sum of three exponential functions of the form

$$I(t) = \sum_{i=1}^{3} \alpha_i \cdot e^{-t/\tau_i} \tag{8}$$

was used to fit the decay as this proved to be the model that provided the best fit with the least number of exponentials, and is in line with what is reported by other groups for $CsPbBr_3$ QDs [39]. Table 1 displays the parameters of this fit. Decay constants of around 1, 8 and 46 ns were obtained, with weights of 52, 42 and 7%, respectively, placing the average lifetime according to (6) at 25.4 ns. This corresponds to a bandwidth of ~11 MHz as is given by (5), for a power density of ~0.1 mW/cm^2.

Table 1. Parameters for triple-exponential fits to TCSPC measurements

τ_1 (ns)	a_1 (%)	τ_2 (ns)	a_2 (%)	τ_3 (ns)	a_3 (%)	$\tilde{\tau}$ (ns)[a]	Bwdth (MHz)[b]
1.2	52%	7.7	41%	46.2	7%	25.4	10.8

As explained in section 2, the frequency responses under LED and LD pumping were fitted with the model described by (2) – (4) and also assumed a triple exponential decay. The optical bandwidths for the color converters, and the average luminescence lifetimes, were extracted from the frequency response fits at −6 dB and plotted *vs* power density in Fig. 7.

We can observe that at 0.1 mW/cm^2 the bandwidth is around 11 MHz (average lifetime of ~25.4 ns). This doubles (halves) to around 20 MHz (~13 ns) under μLED excitation for a ~10^3 factor increase in excitation power density. The relatively low bandwidth at very low pump density (TCSPC data) is attributed to a re-absorption effect, which is known to artificially slow the overall emission process [8]. Under μLED pumping the bandwidth continuously increases with the power density P_d at a rate proportional to $P_d^{0.11}$. Two reasons can explain this increase with P_d: (i) the overall reabsorption effect diminishes, and (ii) the probability for radiative recombination increases as sub-levels of the ground state involved in the transition get populated [11]. However, above 2 W/cm^2 the bandwidth stabilizes around 21-22 MHz, probably as the color converter nears transparency at its emission wavelength. Such bandwidth values correspond to an average lifetime of 12-13 ns. Under LD pumping, the bandwidth increases again but at a faster rate, proportional to $P_d^{0.55}$, until 2 kW/cm^2, i.e. a power slope five times than at the lower μLED pumping density regime. Beyond this point, the bandwidth still increases, but at a slower rate, proportional to $P_d^{0.17}$. The color converter's bandwidth at 7.15 kW/cm^2 is 41 MHz. Using

Optical Materials EXPRESS

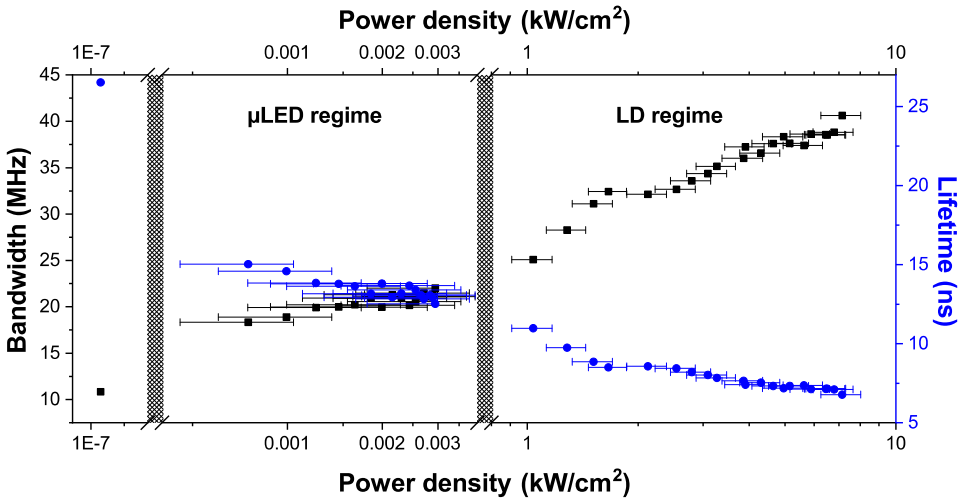

Fig. 7. Bandwidth and lifetime for increasing power densities. Lower values for the TCSPC measurement; middle values for μLED excitation; higher values for LD excitation.

Eq. (1) it is possible to relate the radiative times at low (< 2 kW/cm^2) and high (> 2 kW/cm^2) power densities, by dividing the (normalized) forward efficiencies and using the lifetimes from Fig. 7. From this we infer that the radiative lifetime at high power densities is 1.3 times that at low power density, which indicates that the radiative lifetime may increase. Given that the bandwidth still increases at high power densities (average lifetime decreases), despite a possible increase in radiative lifetime, the acceleration in this regime can be ascribed to more dominant non-radiative recombination, probably caused by multi-excitonic and temperature effects [11,40]. This increase in non-radiative recombination also explains the decrease in the relative efficiency discussed in section 3.1. Therefore the difference in behaviour between μLED and LD pumping comes from the significantly difference in excitation density.

3.3. OFDM VLC link at 2 different pump densities using the color converter

Using the μLED and LD as excitation sources, data communication tests over 10 cm were conducted with the color converter pumped in different density regimes. DC biased Optical Orthogonal Frequency Division Multiplexing (DCO-OFDM) was used as the modulation scheme. DCO-OFDM enables an optimization of the use of the channel bandwidth by dividing it into several orthogonal carrier frequencies, giving different weights to each one to accommodate the Signal-to-Noise-Ratio (SNR) [41]. The μLED was DC driven at 90 mA (2.15 W/cm^2 excitation power density) and the LD at 150 mA (7.15 kW/cm^2 excitation power density), corresponding to color converter bandwidths of 21 and 41 MHz, respectively. For the DCO-OFDM signal, an arbitrary waveform was generated offline using a MatLab script. The waveform was then loaded onto an Arbitrary Waveform Generator, which provided the AC part of the signal to a Bias-T, while a power source supplied a DC component; this drove the excitation source. The samples down-converted the blue emission to green, which was then focused onto an Avalanche Photodiode (APD), which detected and transmitted the signal to a computer, where it was demodulated and analyzed.

For μLED pumping, the APD had an area of 19.6 mm^2 and a bandwidth of 100 MHz. Because LD pumping led to a higher color-converted optical power and bandwidth, a smaller, faster APD was used: 0.78 mm^2 with a 200 MHz bandwidth. The SNR for the channel is plotted as a function of the frequency for the μLED (red) and LD (black) excited color converter in Fig. 8. The use of

Optical Materials EXPRESS

a different APD explains the higher (10 dB) SNR at low frequency for μLED pumping. However, in both cases the color-converter is the limiting parameter for the channel bandwidth and it can be seen that as the frequency increases, the frequency response drops much faster under μLED excitation than under LD excitation. Consequently, under μLED pumping, the overall channel bandwidth that can be used, defined as the range where the SNR is positive, for DCO-OFDM is 75 MHz but it is up to 160 MHz for LD pumping. For LD pumping, the SNR is also above zero in the 185-200 MHz range, which can therefore be used for loading some information.

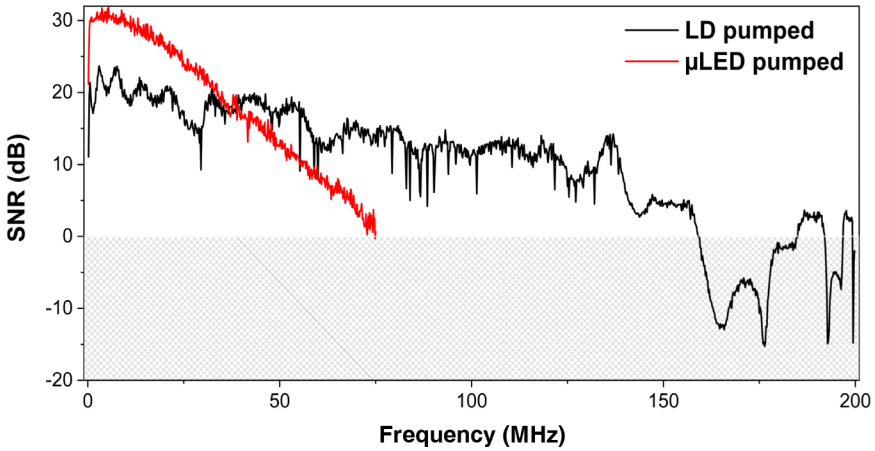

Fig. 8. SNR plot for the color converter under μLED and LD excitation used to determine the available bandwidth. The area in gray cross-hatch corresponds to unusable carriers for communications.

The Bit Error Rate (BER) as a function of data rates is plotted in Fig. 9(a), for both μLED and LD pumping. Using a long pass filter with cut-off below 500 nm, the blue emission from the source (μLED or LD) is filtered out and only the color-converted emission reaches the detector; similar measurements were performed without any filtering of the blue light. Error-free transmission is defined for a BER below 3.8E-3, typical for DCO-ODFM considering Forward Error Correction can be implemented.

Enabled by the larger bandwidth under LD pumping, the color converter alone reaches an estimated 560 Mb/s, while under μLED pumping that value is lower at 380 Mb/s. Given that under the LD pumping the bandwidth of the color converter is larger (as well as output optical power), it is understandable that the data rate is higher. While in terms of raw capability for data transmission, a direct laser diode is an ideal choice, the color-converter approach enables the utilisation of a unique pump source (blue or UV) for the generation of different wavelengths, which is the approach taken in many lighting and display applications. Spectrally narrow color converters (including in the green) are advantageous in this context to obtain a wide gamut, or even white light, efficiently.

Without the long pass filter, the spectral contribution of non-absorbed pump light also reaches the APD, enabling even higher error free data rates. In Fig. 9(b), the illuminance spectrum under μLED pumping is shown. The illuminance spectra were acquired using a Labsphere E-1000 Irradiance Head placed at the detection point, connected to an Ocean Optics USB 4000 spectrometer. The pump contribution between 390 nm and 480 nm is 0.52 lm/cm^2, whilst the green contribution between 380 and 800 nm is of 0.11 lm/cm^2. This relatively large blue component is mainly due to the set-up implementation leading a non-negligible amount of pump light not interacting with the sample also collected by the optical system. With this pump contribution, not only there is more power reaching the APD, the overall bandwidth available for

Optical Materials EXPRESS

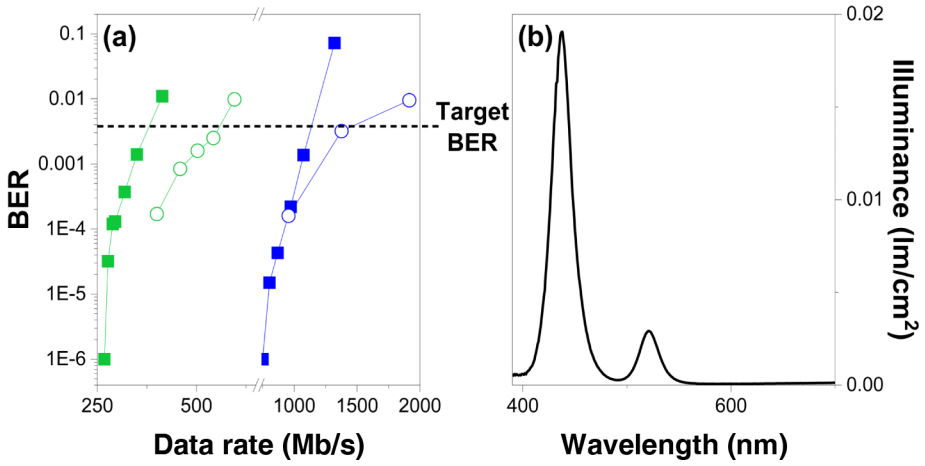

Fig. 9. (a) - BER vs data rates, using a μLED pump (squares) and a LD pump (circles) and with (blue) and without (green) a pump source contribution. (b) Illuminance spectrum illustrating the higher contribution from the LED for the 1.14 Gb/s result.

communications increases, as a consequences of the faster dynamics of the μLED [42] and LDs [43,44]. In turn the data rates reach 1.14 and 1.5 Gb/s for μLED and LD excitation, respectively.

4. Conclusions

For the first time to our knowledge, $CsPbBr_3$ QDs in Cs_4PbBr_6 crystals were used as a fast color converter (bandwidth of a few tens of MHz, i.e. 1 to 3 orders of magnitude higher than typical phosphors), with emission at 520 nm, for VLC. Micron-sized crystal powder samples of the $CsPbBr_3$-in-Cs_4PbBr_6 QD material were integrated in a polymeric matrix for excitation by either a μLED or LD. A study of the optical properties at different pump power density regimes (from 0.7 mW/cm^2 to 7.15 kW/cm^2) was conducted. The spectral emission of the color converter, peaking at 522 nm, is narrow, with a typical 18 nm FWHM, and independent of the pump power density. The relative efficiency measured by our set-up in the forward direction is estimated at 10% under μLED excitation, an efficiency that is maintained only at low LD excitation powers, after which it decreases to below 5% at 7.15 kW/cm^2. At low pump density and up to 3 W/cm^2, the bandwidth continuously increases while the efficiency does not significantly decrease. This bandwidth increase is attributed to band filling, which reduces re-absorption and increases the probability for radiative recombination. The bandwidth at 3 W/cm^2 is 22 MHz, corresponding to an average lifetime of 13 ns. Such a lifetime is shorter than II-VI QD converters emitting at similar wavelengths and pumped in similar conditions [8]. The efficiency is seen to drop significantly at higher pump densities (> 2 kW/cm^2) while the bandwidth increases significantly, at twice the rate than what is seen at low density. The bandwidth reaches 41 MHz, which corresponds to a lifetime below 7 ns, at 7 kW/cm^2. While the efficiency drops in this density regime the output power still increases. Therefore, LD pumping leads to higher optical power and bandwidth, which are beneficial for VLC, although this comes at the cost of overall efficiency.

Using either the μLED or LD as a pump source, free-space DCO-OFDM communication over 10 cm was demonstrated, achieving data rates for light from the color converter alone of 380 and 560 Mb/s, respectively. The higher data rate for LD pumping is linked to the higher optical power and bandwidths. When the optical filter blocking the unabsorbed, scattered pump light is

Optical Materials EXPRESS

removed, both pump light and color converted light are detected by the system. In this case, data rates of 1.14 and 1.5 Gb/s are achieved for μLED and LD excitation respectively.

Funding

Engineering and Physical Sciences Research Council (EPSRC) (EP/K00042X/1, EP/P0274X/2).

Acknowledgments

The authors wish to acknowledge Dr. E. Xie (Institute of Photonics, University of Strathclyde) for the μLED fabrication; Dr Paul Edwards, Dr Jochen Bruckbauer and Prof Rob Martin (Physics Department, University of Strathclyde) for the assistance in acquiring the SEM images, CL characterization and PLQY measurements; Ms. Abeer Alghamdi and Dr Olaf Rolinski (Physics Department, University of Strathclyde) for the assistance with acquiring the PLE spectra.

References

1. K. Rae, C. Foucher, B. Guilhabert, M. S. Islim, L. Yin, D. Zhu, R. A. Oliver, D. J. Wallis, H. Haas, N. Laurand, and M. D. Dawson, "InGaN μLEDs integrated onto colloidal quantum dot functionalized ultra-thin glass," Opt. Express **25**(16), 19179 (2017).
2. C. Foucher, M. I. Sufyan, B. J. E. Guilhabert, S. Videv, S. Rajbhandari, A. G. Diaz, H. Chun, D. A. Vithanage, G. A. Turnbull, I. D. W. Samuel, G. Faulkner, D. C. O'Brien, H. Haas, N. Laurand, and M. D. Dawson, "Flexible Glass Hybridized Colloidal Quantum Dots for Gb/s Visible Light Communications," IEEE Photonics J. **10**(1), 1–11 (2018).
3. J. Grubor, S. C. J. Lee, K. Langer, T. Koonen, and J. W. Walewski, "Wireless High-Speed Data Transmission with Phosphorescent White-Light LEDs," in *33rd European Conference and Exhibition of Optical Communication - Post-Deadline Papers (Published 2008)* (2007), pp. 1–2.
4. C. H. Yeh, Y. F. Liu, C. W. Chow, Y. Liu, P. Y. Huang, and H. K. Tsang, "Investigation of 4-ASK modulation with digital filtering to increase 20 times of direct modulation speed of white-light LED visible light communication system," Opt. Express **20**(15), 16218–16223 (2012).
5. J. M. M. Santos, B. E. Jones, P. J. Schlosser, S. Watson, J. Herrnsdorf, B. Guilhabert, J. J. D. McKendry, J. De Jesus, T. A. Garcia, M. C. Tamargo, A. E. Kelly, J. E. Hastie, N. Laurand, and M. D. Dawson, "Hybrid GaN LED with capillary-bonded II–VI MQW color-converting membrane for visible light communications," Semicond. Sci. Technol. **30**(3), 035012 (2015).
6. J. M. M. Santos, S. Rajbhandari, D. Tsonev, H. Chun, B. Guilhabert, A. B. Krysa, A. E. Kelly, H. Haas, D. C. O'Brien, N. Laurand, and M. D. Dawson, "Visible light communication using InGaN optical sources with AlInGaP nanomembrane down-converters," Opt. Express **24**(9), 10020 (2016).
7. D. A. Vithanage, A. L. Kanibolotsky, S. Rajbhandari, P. Manousiadis, M. Sajjad, H. Chun, G. Faulkner, D. C. O'Brien, P. Skabara, I. Samuel, and G. Turnbull, "Polymer colour converter with very high modulation bandwidth for visible light communications," J. Mater. Chem. C **5**(35), 8916–8920 (2017).
8. M. F. Leitao, J. M. M. Santos, B. J. E. Guilhabert, S. Watson, A. E. Kelly, M. S. Islim, H. Haas, M. D. Dawson, and N. Laurand, "Gb/s Visible Light Communications with Colloidal Quantum Dot Color Converters," IEEE J. Sel. Top. Quantum Electron. **23**(5), 1–10 (2017).
9. I. Dursun, C. Shen, M. R. Parida, J. Pan, S. P. Sarmah, D. Priante, N. Alyami, J. Liu, M. I. Saidaminov, M. S. Alias, A. L. Abdelhady, T. K. Ng, O. F. Mohammed, B. S. Ooi, and O. M. Bakr, "Perovskite Nanocrystals as a Color Converter for Visible Light Communication," ACS Photonics **3**(7), 1150–1156 (2016).
10. S. Mei, X. Liu, W. Zhang, R. Liu, L. Zheng, R. Guo, and P. Tian, "High-Bandwidth White-Light System Combining a Micro-LED with Perovskite Quantum Dots for Visible Light Communication," ACS Appl. Mater. Interfaces **10**(6), 5641–5648 (2018).
11. F. T. Rabouw and C. de Mello Donega, "Excited-State Dynamics in Colloidal Semiconductor Nanocrystals," Top. Curr. Chem. **374**(5), 58 (2016).
12. L. Protesescu, S. Yakunin, M. I. Bodnarchuk, F. Krieg, R. Caputo, C. H. Hendon, R. X. Yang, A. Walsh, and M. V. Kovalenko, "Nanocrystals of Cesium Lead Halide Perovskites ($CsPbX_3$, X = Cl, Br, and I): Novel Optoelectronic Materials Showing Bright Emission with Wide Color Gamut," Nano Lett. **15**(6), 3692–3696 (2015).
13. J. Song, J. Li, X. Li, L. Xu, Y. Dong, and H. Zeng, "Quantum Dot Light-Emitting Diodes Based on Inorganic Perovskite Cesium Lead Halides ($CsPbX_3$)," Adv. Mater. **27**(44), 7162–7167 (2015).
14. J. Li, X. Yuan, P. Jing, J. Li, M. Wei, J. Hua, J. Zhao, and L. Tian, "Temperature-dependent photoluminescence of inorganic perovskite nanocrystal films," RSC Adv. **6**(82), 78311–78316 (2016).
15. C. Li, Z. Zang, C. Han, Z. Hu, X. Tang, J. Du, Y. Leng, and K. Sun, "Highly compact $CsPbBr_3$ perovskite thin films decorated by ZnO nanoparticles for enhanced random lasing," Nano Energy **40**, 195–202 (2017).
16. C. Li, Z. Zang, W. Chen, Z. Hu, X. Tang, W. Hu, K. Sun, X. Liu, and W. Chen, "Highly pure green light emission of perovskite $CsPbBr_3$ quantum dots and their application for green light-emitting diodes," Opt. Express **24**(13), 15071–15078 (2016).

Optical Materials EXPRESS

17. D. Yan, T. Shi, Z. Zang, T. Zhou, Z. Liu, Z. Zhang, J. Du, Y. Leng, and X. Tang, "Ultrastable $CsPbBr_3$ Perovskite Quantum Dot and Their Enhanced Amplified Spontaneous Emission by Surface Ligand Modification," Small **15**, 1901173 (2019).
18. P. U. Alves, I. M. Watson, N. Laurand, and M. D. Dawson, "Water Resistant Caesium Lead Bromide Crystal Composites," *2018 IEEE British and Irish Conference on Optics and Photonics (BICOP)*, London, United Kingdom, 2018, 1–4, doi: 10.1109/BICOP.2018.8658335.
19. Y. Wang, D. Yu, Z. Wang, X. Li, X. Chen, V. Nalla, H. Zeng, and H. Sun, "Solution-Grown $CsPbBr_3/Cs_4PbBr_6$ Perovskite Nanocomposites: Toward Temperature-Insensitive Optical Gain," Small **13**(34), 1701587 (2017).
20. Q. A. Ackkerman, A. L. Abdelhady, and L. Manna, "Zero-Dimensional Cesium Lead Halides: History, Properties, and Challenges," J. Phys. Chem. Lett. **9**(9), 2326–2337 (2018).
21. L. N. Quan, R. Quintero-Bermudez, O. Voznyy, G. Walters, A. Jain, J. Zhangming Fan, X. Zheng, Z. Yang, and E. H. Sargent, "Highly Emissive Green Perovskite Nanocrystals in a Solid State Crystalline Matrix," Adv. Mater. **29**(21), 1605945 (2017).
22. X. Chen, F. Zhang, Y. Ge, L. Shi, S. Huang, J. Tang, Z. Lv, L. Zhang, B. Zou, and H. Zhong, "Centimeter-Sized Cs_4PbBr_6 Crystals with Embedded $CsPbBr_3$ Nanocrystals Showing Superior Photoluminescence: Nonstoichiometry Induced Transformation and Light-Emitting Applications," Adv. Funct. Mater. **28**(16), 1706567 (2018).
23. X. Li, F. Cao, D. Yu, J. Chen, Z. Sun, Y. Shen, Y. Zhu, L. Wang, Y. Wei, Y. Wu, and H. Zeng, "All Inorganic Halide Perovskites Nanosystem: Synthesis, Structural Features, Optical Properties and Optoelectronic Applications," Small **13**(9), 1603996 (2017).
24. P. R. Edwards, L. K. Jagadamma, J. Bruckbauer, C. Liu, P. Shields, D. Allsopp, T. Wang, and R. W. Martin, "High-resolution cathodoluminescence hyperspectral imaging of nitride nanostructures," Microsc. Microanal. **18**(6), 1212–1219 (2012).
25. J. Yin, Y. Zhang, A. Bruno, C. Soci, O. M. Bakr, J. L. Brédas, and O. F. Mohammed, "Intrinsic Lead Ion Emissions in Zero-Dimensional Cs_4PbBr_6 Nanocrystals," ACS Energy Lett. **2**(12), 2805–2811 (2017).
26. M. Nikl, E. Mihokova, and K. Nitsch, "Photoluminescence & decay kinetics of Cs_4PbCl_6 single crystals," Solid State Commun. **84**(12), 1089–1092 (1992).
27. M. Nikl, K. Nitsch, I. Velicka, J. Hybler, K. Polak, and T. Fabian, "Photoluminescence of KPb_2Cl_5," Phys. Status Solidi B **168**(1), K37–K42 (1991).
28. M. Nikl, K. Nitsch, and K. Polak, "Photoluminescence of $RbPb_2Cl_5$," Phys. Status Solidi B **166**(2), 511–518 (1991).
29. M. Nikl, E. Mihokova, K. Nitsch, F. Somma, C. Giampaolo, G. Pazzi, P. Fabeni, and S. Zazubovich, "Photoluminescence of Cs_4PbBr_6 crystals and thin films," Chem. Phys. Lett. **306**(5-6), 280–284 (1999).
30. Y. Zhang, M. I. Saidaminov, I. Dursun, H. Yang, B. Murali, E. Alarousu, E. Yengel, B. A. Alshankiti, O. M. Bakr, and O. F. Mohammed, "Zero-Dimensional Cs_4PbBr_6 Perovskite Nanocrystals," J. Phys. Chem. Lett. **8**(5), 961–965 (2017).
31. S. Seth and A. Samanta, "Photoluminescence of Zero-Dimensional Perovskites and Perovskite-Related Materials," J. Phys. Chem. Lett. **9**(1), 176–183 (2018).
32. M. Nikl, K. Nitsch, E. Mihokova, K. Polak, P. Fabeni, G. P. Pazzi, M. Gurioli, R. Phani, S. Santucci, A. Scacco, and F. Somma, "Optical properties of Pb^{2+} - based aggregated phases in CsBr Thin film and single crystal matrices," Radiat. Eff. Defects Solids **150**(1-4), 341–345 (1999).
33. M. Nikl, K. Nitsch, J. Chval, F. Somma, A. R. Phani, S. Santucci, C. Giampaolo, P. Fabeni, G. P. Pazzi, and X. Q. Feng, "Optical and structural properties of ternary nanoaggregates in CsI-PbI_2 co-evaporated thin films," J. Phys.: Condens. Matter **12**(8), 1939–1946 (2000).
34. A. E. Siegman, "How to (Maybe) Measure Laser Beam Quality," in *DPSS (Diode Pumped Solid State) Lasers: Applications and Issues* (OSA, 1998), p. MQ1.
35. Z. Gong, S. Jin, Y. Chen, J. McKendry, D. Massoubre, I. M. Watson, E. Gu, and M. D. Dawson, "Size-dependent light output, spectral shift, and self-heating of 400 nm InGaN light-emitting diodes," J. Appl. Phys. **107**(1), 013103 (2010).
36. J. R. Lakowicz, *Principles of Fluorescence Spectroscopy* (Springer, 2006).
37. E. Jang, S. Jun, H. Jang, J. Lim, B. Kim, and Y. Kim, "White-light-emitting diodes with quantum dot color converters for display backlights," Adv. Mater. **22**(28), 3076–3080 (2010).
38. E. F. Schubert, *Light-Emitting Diodes*, 2nd ed. (Cambridge University Press, 2003).
39. N. S. Makarov, S. Guo, O. Isaienko, W. Liu, I. Robel, and V. I. Klimov, "Spectral and Dynamical Properties of Single Excitons, Biexcitons, and Trions in Cesium-Lead-Halide Perovskite Quantum Dots," Nano Lett. **16**(4), 2349–2362 (2016).
40. L. Xu, J. Chen, J. Song, J. Li, J. Xue, Y. Dong, B. Cai, Q. Shan, B. Han, and H. Zeng, "Double-Protected All-Inorganic Perovskite Nanocrystals by Crystalline Matrix and Silica for Triple-Modal Anti-Counterfeiting Codes," ACS Appl. Mater. Interfaces **9**(31), 26556–26564 (2017).
41. D. Tsonev, H. Chun, S. Rajbhandari, J. J. D. McKendry, S. Videv, E. Gu, M. Haji, S. Watson, A. E. Kelly, G. Faulkner, M. D. Dawson, H. Haas, and D. O'Brien, "A 3-Gb/s single-LED OFDM-based wireless VLC link using a gallium nitride μLED," IEEE Photonics Technol. Lett. **26**(7), 637–640 (2014).
42. M. Islim, R. Ferreira, X. He, E. Xie, S. Videv, S. Viola, S. Watson, N. Bamiedakis, R. Penty, I. White, A. Kelly, E. Gu, H. Haas, and M. D. Dawson, "Towards 10 Gb/s OFDM-based Visible Light Communication using a GaN Violet micro-LED," Photonics Res. **5**(2), A35–A43 (2017).

Optical Materials EXPRESS

43. C. Lee, C. Zhang, M. Cantore, R. M. Farrell, S. H. Oh, T. Margalith, J. S. Speck, S. Nakamura, J. E. Bowers, and S. P. DenBaars, "4 Gbps direct modulation of 450 nm GaN laser for high-speed visible light communication," Opt. Express **23**(12), 16232–16237 (2015).
44. S. Watson, M. Tan, S. P. Najda, P. Perlin, M. Leszczynski, G. Targowski, S. Grzanka, and A. E. Kelly, "Visible light communications using a directly modulated 422 nm GaN laser diode," Opt. Lett. **38**(19), 3792–3794 (2013).